

## Experimental and Numerical Analysis of Punching Shear of GFRP-RC Slabs

Aroob Al-Ateyat <sup>1</sup>, Samer Barakat <sup>1\*</sup>, M. Talha Junaid <sup>1</sup>, Salah Altoubat <sup>1</sup>,  
Mohamed Maalej <sup>1</sup>, Raghad Awad <sup>1</sup>

<sup>1</sup> Civil and Environmental Engineering Department, College of Engineering, University of Sharjah, Sharjah, United Arab Emirates.

Received 19 October 2024; Revised 12 December 2024; Accepted 20 December 2024; Published 6 January 2025

### Abstract

This study investigates the punching shear behavior of Glass Fiber-Reinforced Polymer (GFRP)-reinforced concrete slabs, addressing critical gaps in current design guidelines for high-strength concrete (HSC). The objective is to evaluate the impact of concrete strength, including normal-strength concrete (NSC, 30 MPa) and HSC (60 and 90 MPa), on the punching shear resistance, bridging the lack of experimental data that limits the use of HSC in FRP-reinforced slabs. The research employs experimental testing on three full-scale slab specimens (1.5 m × 1.5 m × 0.1 m) under concentric monotonic loading until failure, coupled with Finite Element Analysis (FEA) using the Concrete Damage Plasticity (CDP) model in ABAQUS. Key findings reveal that increasing concrete strength moderately enhances punching shear resistance by 5.6% and 8.9% for 100% and 200% strength increases, respectively. The FEA model successfully replicates load-deflection behavior, crack patterns, and failure mechanisms with less than a 3% deviation from experimental results. This study enriches the literature with experimental data on GFRP-reinforced slabs using HSC and verifies FEA as a robust design tool for engineers. The findings contribute to developing comprehensive design guidelines for FRP-reinforced slabs subjected to punching shear in high-strength applications.

**Keywords:** GFRP-Reinforced Concrete Slabs; Punching Shear; High-Strength Concrete (HSC); FEA; CDP; ABAQUS.

## 1. Introduction

The flat plate system is widely used in structures such as parking garages due to its simplicity and adaptability. However, steel-reinforced concrete faces durability challenges in corrosive environments, where steel corrosion significantly reduces structural capacity and lifespan. Fiber-reinforced polymer (FRP) bars present a promising alternative, offering corrosion resistance, lightweight properties, non-conductivity, and a high strength-to-weight ratio. These advantages have led to their application in bridge decks, underground works, and parking structures [1-3]. Nevertheless, punching shear remains a critical concern in flat plates, as inadequate consideration of this failure mode can lead to catastrophic outcomes. Existing studies have highlighted the challenges of punching shear in GFRP-reinforced slabs. Nguyen-Minh & Rovňák (2013) [4] reported that GFRP-reinforced slabs exhibited 38% lower punching shear resistance and 34% wider cracks than steel-reinforced slabs. Ju et al. (2018) [5] demonstrated that reinforcement ratios enhance punching shear capacity, but predictive equations in existing codes often overestimate strength, particularly for slabs supported by reinforced concrete girders. Similarly, Duan and Zhang (2024) [6] showed that increasing reinforcement ratios in CFRP-reinforced slabs improved shear capacity and reduced deflection.

\* Corresponding author: [sbarakat@sharjah.ac.ae](mailto:sbarakat@sharjah.ac.ae)



<http://dx.doi.org/10.28991/CEJ-SP2024-010-017>



© 2024 by the authors. Licensee C.E.J., Tehran, Iran. This article is an open access article distributed under the terms and conditions of the Creative Commons Attribution (CC-BY) license (<http://creativecommons.org/licenses/by/4.0/>).

Other studies have investigated the influence of design parameters, such as column size, aspect ratio, and span-to-depth ratio, on punching shear resistance. Talha Junaid et al. (2024) [7] found that increasing column size by 20% improved punching shear capacity by 25%, while Alkhatabi et al. (2024) [8] highlighted that an increase in column–aspect ratio reduced punching shear stress by 27%. Both studies emphasized that existing design codes, such as ACI 440.11-22 [9], CAN/CSA S806-12 [10], and JSCE-97 [11], require refinement to address these parameters accurately.

Regarding the effect of concrete strength on punching shear resistance, most studies have focused on NSC, including the works of Lee et al. (2010) [12], Hassan et al. (2015) [13], Nguyen-Minh & Rovňák (2013) [4], and Ju et al. (2018) [5]. Few studies, however, have explored HSC. For instance, Hassan et al. (2013) [14] examined NSC (34 MPa) and HSC (76 MPa), along with other parameters, such as effective depth and reinforcement ratio, on punching shear behavior. Their study confirmed that higher reinforcement ratios combined with HSC significantly improved punching shear capacity. Zhang et al. (2005) [15] showed that while HSC (86–98 MPa) moderately enhanced shear capacity, reinforcement ratio and column dimensions were the dominant factors. Hussein and El-Salakawy (2018) [16] further demonstrated that using HSC (80–87 MPa) increased cracking loads and punching capacity by 26% and 22%, respectively, when compared to NSC. Despite these findings, there remains a significant lack of experimental studies on HSC in GFRP-reinforced slabs. Databases compiled by Xu & Shi (2024) [17] and Alateyat et al. (2024) [18], comprising 189 and 272 experimental samples, respectively, revealed that less than 10% of tested slabs utilized HSC. Prominent design codes, such as ACI 440.11-22 [9], CAN/CSA S806-12 [10], and JSCE-97 [11], impose limitations on the use of HSC due to insufficient experimental evidence on its punching shear behavior.

In addition to the scarcity of experimental data, the underlying mechanisms of punching shear and the associated design parameters require further investigation. Finite element analysis (FEA) has emerged as a valuable tool to complement experimental findings by offering insights into structural performance, such as crack development, deformations, and failure modes—areas that experimental methods may not fully capture. Significant progress has been made in modeling two-way shear in FRP-reinforced slabs. For instance, the works of Madkour et al. (2022) [19] and Al-Rousan et al. (2020) [20] validated FEA models against experimental data, demonstrating the capability of these models to capture punching shear behavior accurately. These studies also conducted parametric analyses to evaluate design parameters, providing a deeper understanding of the structural behavior of FRP-reinforced slabs.

Given the limited experimental studies and lack of detailed investigations into the underlying mechanisms of punching shear in GFRP-reinforced slab-column connections with HSC, this study conducts a comprehensive experimental analysis. The research examines the behavior of concentrically loaded GFRP-reinforced concrete slabs made with NSC and HSC, subjected to punching shear. Additionally, FEA is performed using ABAQUS software to provide deeper insights into such connections' behavior, analysis, and design. By combining experimental findings and numerical simulations, this study enriches the existing literature with valuable data on GFRP-reinforced slabs using HSC. It establishes FEA as a reliable design tool for engineers. The findings aim to advance the development of comprehensive design guidelines for FRP-reinforced slabs in high-strength applications. The process followed in this study is illustrated in Figure 1.

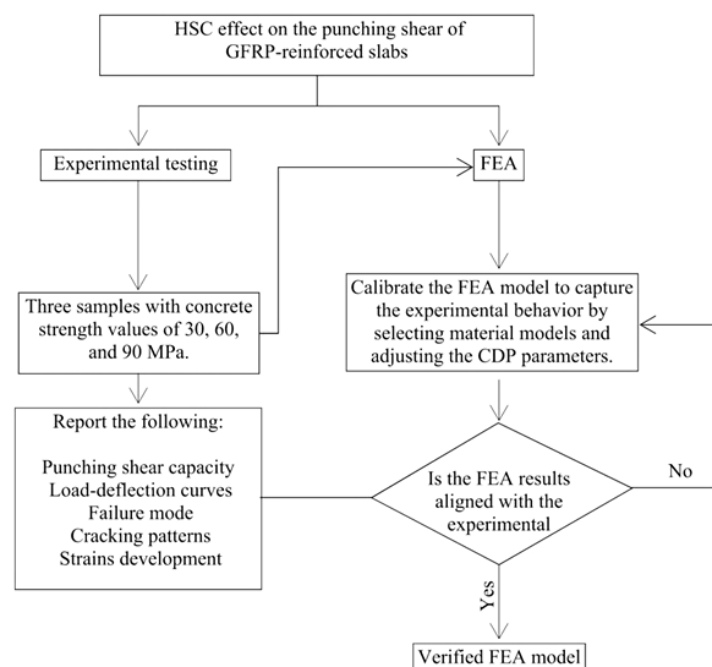


Figure 1. Study flow chart

## 2. Specimens' Details

Three slab specimens, each measuring  $1.5 \times 1.5$  m with a uniform thickness of 100 mm and column dimensions of  $150 \times 150$  mm, were constructed and tested for punching shear, as depicted in Figure 2. The slabs were reinforced with 12 GFRP bars in each direction, spaced at 131 mm center-to-center. Designed according to ACI 440.11-22 [9], the slabs were reinforced to resist flexural loads exceeding the nominal punching shear capacity, ensuring that punching shear governed the failure mode. The load was applied via a square stub column at the center of each slab. This column was reinforced with four vertical steel bars (20 mm diameter) and three horizontal ties (8 mm diameter) to prevent column failure. Detailed geometry and reinforcement specifications are shown in Figure 2 and Table 1.

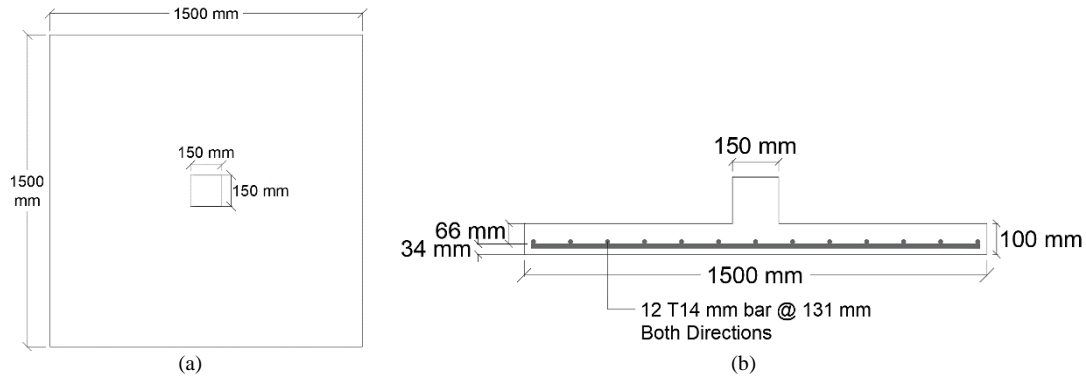


Figure 2. Geometry and reinforcement scheme for the specimens: (a) Top view, (b) Side view

Table 1. Test specimens' details.

Sample ID	Measured $f'_c$	Effective depth, (d)		Reinforcement	
	MPa	mm	Type	Spacing (S, mm)	Ratio ( $\rho\%$ )
G-30-1.8	35				
G-60-1.8	65	66	GFRP	131	1.8
G-90-1.8	103				

The specimens were labeled as G-CS-1.8, where “G” denotes GFRP reinforcement, “CS” specifies the targeted concrete strength (30, 60, or 90 MPa), and “1.8” represents the reinforcement ratio.

## 3. Experimental Testing

### 3.1. Materials

The test slabs were cast using normal-weight, ready-mixed concrete with 30, 60, and 90 MPa target compressive strengths at 28 days. The actual compressive strengths measured on the testing day were 35, 64, and 103 MPa. The reinforcement bars used were Grade III with an elastic modulus ( $E$ )  $\geq 60$  GPa, as per ASTM D8505-23 [21], supplied by MateenBars. These deformed bars, designed to enhance the bond between reinforcement and concrete, had a diameter of 14 mm, an ultimate tensile strength of approximately 1000 MPa, and an ultimate tensile strain of 0.0167.

### 3.2. Test Setup and Instrumentation

The slabs were simply supported on a rigid steel frame along all four edges and subjected to a concentric load, applied monotonically in displacement control mode at 0.015 mm/sec until failure. The load was delivered through a 150 mm x 150 mm column using a hydraulic actuator with a 1000 kN capacity, as shown in Figure 3.



Figure 3. Test setup

Strain gauges were mounted on the reinforcement bars to measure strains, positioned at  $2d$  from the column face, where  $d$  is the effective slab depth (Figure 4). Vertical deflections were monitored using Linear Variable Displacement Transducers (LVDTs) placed at mid-span beneath the slab, as illustrated in Figure 5. Crack development was closely observed during testing, with all cracks marked for documentation.

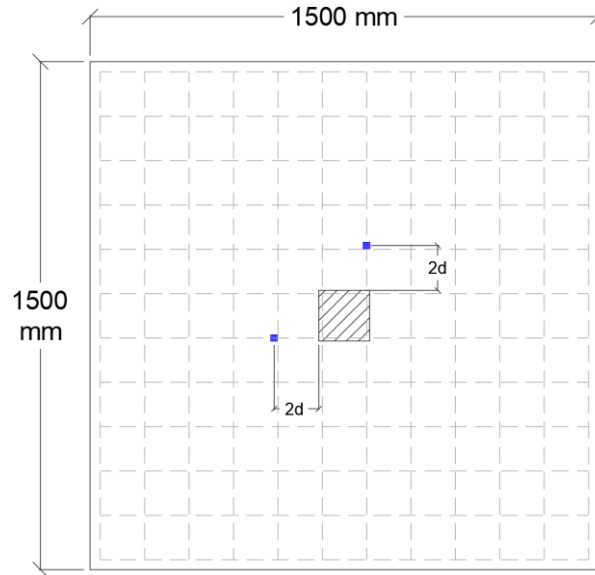


Figure 4. Schematic Mesh instrumentation



Figure 5. LVDT positioning under the slab to measure the vertical deflection

#### 4. Finite Element Analysis

The Concrete Damaged Plasticity Model (CDPM) available in ABAQUS software, Dassault Systemes (2014) [22], was utilized to simulate the punching shear behavior of GFRP-reinforced concrete slabs. This continuum damage model accounts for two primary failure mechanisms: compressive crushing and tensile cracking, governed by the accumulation of plastic strains under compressive and tensile loading. The model incorporates the damage-plasticity behavior of concrete under uniaxial tension and compression. The uniaxial tensile stress-strain relationship shown in Figure 6-a demonstrates a linear response to the tensile failure stress ( $\sigma_{to}$ ), followed by strain softening, indicating the onset of cracking. The uniaxial compressive behavior shown in Figure 6-b begins with a linear-elastic phase up to the initial yield compressive stress ( $\sigma_{co}$ ) and transitions through stress hardening to the ultimate compressive stress ( $\sigma_{cu}$ ). It concludes with strain softening beyond the peak stress. The compression and tension damage parameters ( $d_c$  and  $d_t$ ) are defined by Equations 1 and 2, as shown in Figure 6.

$$\bar{\sigma}_t = \frac{\sigma_t}{(1-d_t)} = E_o(\varepsilon_t^t - \varepsilon_t^{cr}) \quad (1)$$

$$\bar{\sigma}_c = \frac{\sigma_c}{(1-d_c)} = E_o(\varepsilon_c^t - \varepsilon_c^{pl}) \quad (2)$$

In this context, the subscripts  $t$  and  $c$  refer to tension and compression, while  $\bar{\sigma}$  representing effective stress. The damage parameter  $d$  quantifies the degradation of the initial elastic stiffness,  $E_o$  which is typically calculated as  $4700\sqrt{f'_c}$ . The terms  $\varepsilon^t$ ,  $\varepsilon^{pl}$ ,  $\varepsilon^{cr}$  denote the total strain, equivalent plastic strain, and cracking strain, respectively, while  $\varepsilon^{el}$  representing the elastic strain, as illustrated in Figure 6.

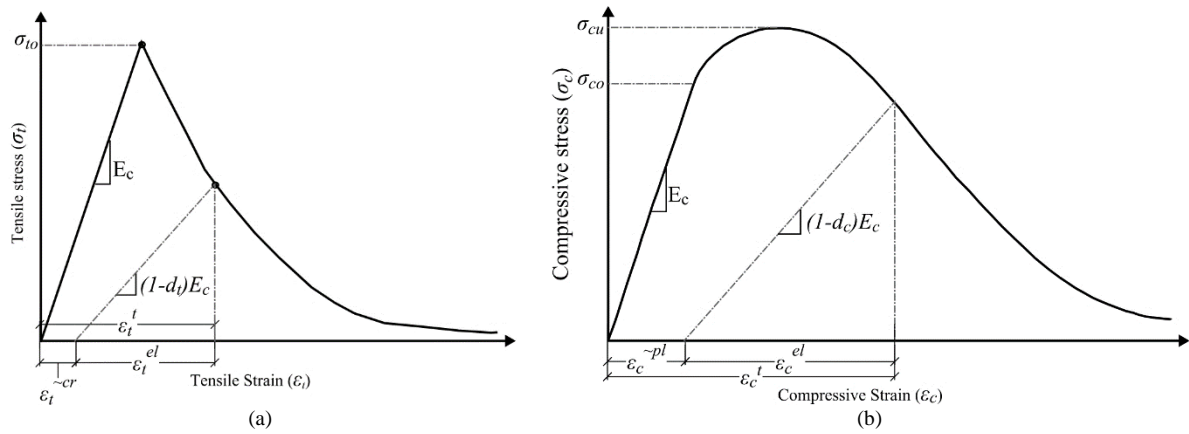


Figure 6. Uniaxial response of concrete (a) Tension, (b) Compression

The software simulates material behavior using the elastic properties within the elastic region. On the other hand, the plastic or cracking strains need to be defined when the material enters the inelastic zone. These strain values are typically calculated by applying Equations 1 and 2 to the stress-strain curve generated from experimental data or using material models commonly found in the literature.

In addition to concrete material modeling, the CDPM is defined through a set of parameters representing the flow potential, yield surface, and viscosity. The yield function is represented by several parameters, including the ratio of biaxial to uniaxial compressive strength ( $\sigma_{bo}/\sigma_{co}$ ), which has a value of 1.16, Dassault Systemes (2014) [22]. The ratio of the second stress invariant (deviatoric stress) to the tensile and compressive meridians ( $K_c$ ) which regulates the shape of the yield surface and its default value (2/3) that is also the most commonly used in the literature.

The flow potential function is defined by the eccentricity of the plastic flow ( $\epsilon$ ), and it has a default value of 0.1 and the dilation angle ( $\phi$ ), which represents the function's slope and can vary between  $30^\circ$  to  $42^\circ$ , as per Voyiadjis and Taqieddin (2009) [23]. The impact of the dilation angle on simulation accuracy was studied by comparing numerical predictions with experimental outcomes. The analysis showed that a dilation angle of  $38^\circ$  most accurately replicated the behavior observed in the experimental tests. The same value was used by Jankowiak and Lodygowski (2005) [24], Mohammadi & Aghayari (2017) [25], and Ren et al. (2014) [26].

The last CDP parameter is the viscosity ( $\mu$ ), a critical time-dependent factor significantly influencing the model's convergence and calculation accuracy. After several trials adjusting the viscosity parameter, a value of 0.001 was found to provide convergence with an adequate running time. A similar approach, adjusting values until achieving convergence, was followed by Surumi et al. (2015) [27] and Nguyen and Livaoğlu (2020) [28]. Table 2 summarizes the adopted values for the CDP parameters.

Table 2. CDPM adopted parameters

Parameter	$\sigma_{bo}/\sigma_{co}$	$K_c$	$\epsilon$	$\phi$	$\mu$
Value	1.16	2/3	0.1	38	0.001

## 4.1. Material Modeling

### 4.1.1. Concrete

The uniaxial compressive behavior of concrete is modeled using the Popovics (1973) [29] approach, selected for its simplicity and effectiveness in representing both normal and high-strength concrete. This model describes the unconfined concrete stress-strain relationship using a single equation applicable beyond the linear elastic phase ( $0.45f'_c$ ). It relies on three key parameters: compressive strength, strain at peak strength, and modulus of elasticity. Equations 3 to 8 define the complete stress-strain curve.

$$\frac{f_c}{f'_c} = \frac{\frac{\epsilon_c}{\epsilon_{co}} r_o}{r_o - 1 + \left(\frac{\epsilon_c}{\epsilon_{co}}\right)^{r_o}} \quad (3)$$

$$r_o = \frac{E_c}{E_c - E_{sec}} \quad (4)$$

$$E_{sec} = \frac{f'_c}{\varepsilon_{co}} \quad (5)$$

$$E_c = 4700\sqrt{f'_c}, \text{ for } f'_c \leq 50 \text{ MPa (NSC)}, [9] \quad (6)$$

$$E_c = 3320\sqrt{f'_c} + 6900, \text{ for } f'_c > 50 \text{ MPa (HSC)}, [28] \quad (7)$$

$$\varepsilon_{co} = (0.01291f'_c + 2.114) \times 10^{-3}, \text{ for } f'_c > 50 \text{ MPa (HSC)}, [29] \quad (8)$$

where  $f'_c$  is the concrete stress at any point on the compression curve, and the corresponding strain value is represented by  $(\varepsilon_c)$ ,  $f'_c$  is the concrete strength,  $\varepsilon_{co}$  the strain value corresponding to the peak concrete compressive strength is taken as 0.002 for NSC with a strength of 50 MPa or less. For concrete strength beyond that (HSC,  $f'_c > 50$  MPa), the strain is calculated using Equation 8, proposed by Hsu & Hsu (1994) [30],  $E_c$  is the elastic modulus,  $E_{sec}$  are the secant elasticity modulus,  $r_o$  is a parameter that relates the initial and secant elasticity moduli.

The resulting stress-plastic strain curves and the corresponding damage parameters for the concrete strengths used are plotted in Figure 7 as input for the FEA model.

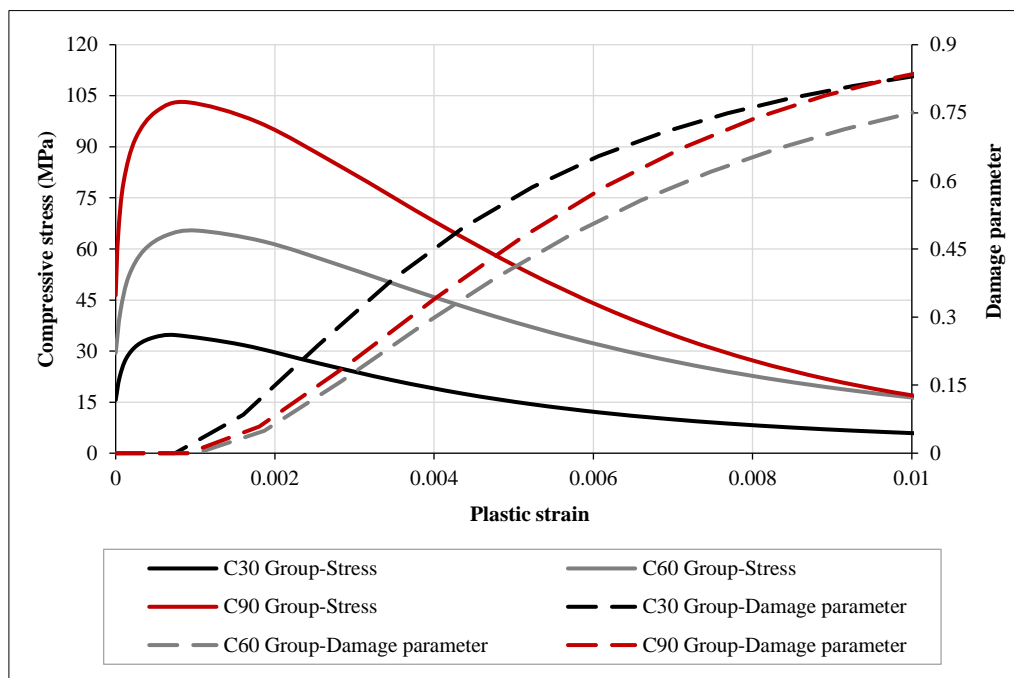


Figure 7. Stress-Plastic strain curves for the considered concrete strengths

The tensile behavior of concrete is modeled as linear elastic up to its tensile strength, defined as one-third of the square root of the concrete compressive strength, following the recommendations of Cornelissen et al. (1986) [31] and utilized by Madkour et al. (2022) [19] and Genikomsou & Polak (2015) [32] for punching shear simulations. The modulus of elasticity determines the slope of this elastic region. The inelastic response is captured using the softening behavior model proposed by Carriera & Chu (1986) [33], selected for its accuracy and realistic representation of tension-stiffening effects. This model uses a single equation for cracking and slippage along reinforcement bars, as described by Equations 9 and 10.

$$\frac{f_t}{f'_t} = \frac{\beta_o \frac{\varepsilon_t}{\varepsilon_{to}}}{\beta_o - 1 + \left(\frac{\varepsilon_t}{\varepsilon_{to}}\right)^{\beta_o}} \quad (9)$$

$$\beta_o = \frac{1}{1 - \frac{f'_c}{\varepsilon_{co} E_c}} \geq 1 \quad (10)$$

where  $\beta_o$  is the shape parameter for the descending part of the curve,  $f'_t$  is the concrete tensile strength,  $\varepsilon_{to}$  is the tensile strain of the concrete corresponding to the tensile strength,  $f_t$  and  $\varepsilon_t$  are the tensile stress and strain at any point on the tensile stress-strain curve.  $E_c$  is the concrete elasticity modulus. Figure 8 presents the tensile stress-strain curves and the corresponding damage parameters used as input for the FEA software.

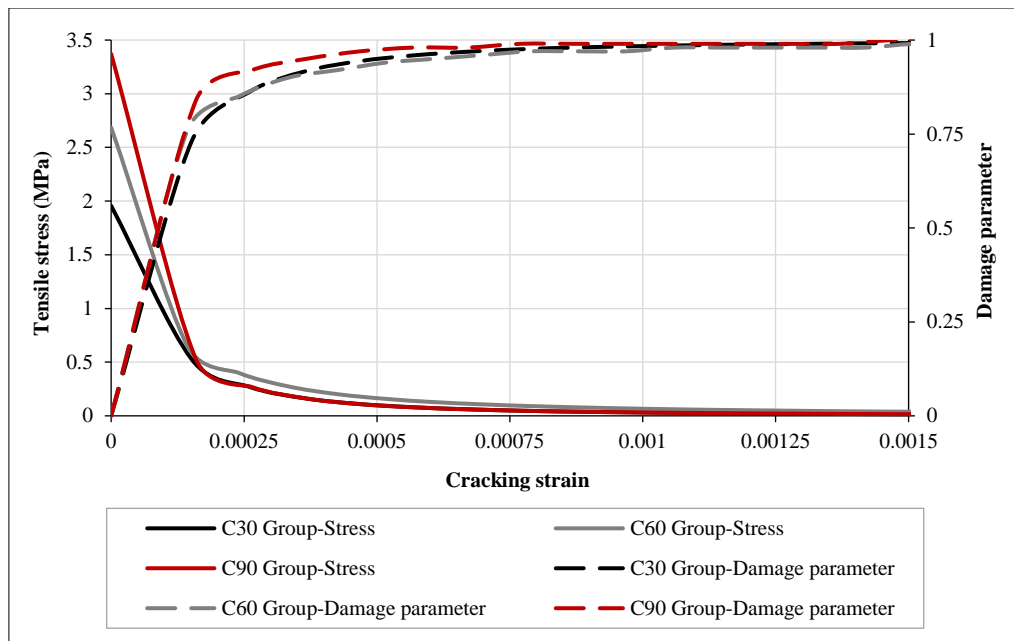


Figure 8. Concrete tensile behavior for the considered concrete strengths

#### 4.1.2. GFRP

The GFRP reinforcement bars were modeled as an elastic-linear isotropic material with the mechanical properties stipulated by the supplier. Figure 9 shows the material model for the GFRP bars; a similar model was used by Al-Rousan et al., (2020) [20] and Demissie & Aure (2022) [34].

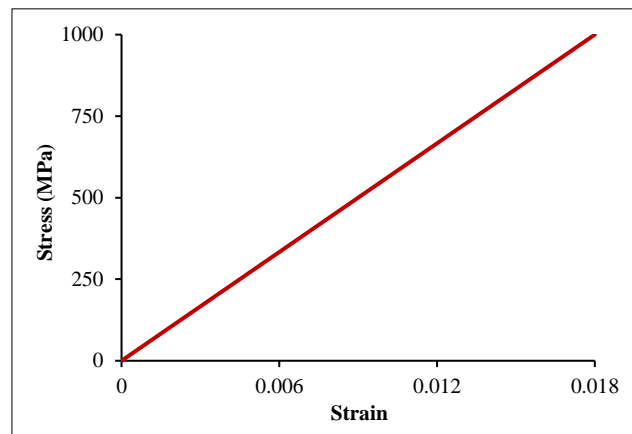


Figure 9. GFRP bars stress-strain model

#### 4.2. Modeling Assumptions

The simulated slabs replicate the dimensions and reinforcement scheme shown in Figure 1. Concrete is modeled using three-dimensional linear solid hexahedral elements with eight nodes (C3D8R). In comparison, the GFRP reinforcement bars are represented by three-dimensional linear truss elements with two nodes (T3D2), each with three degrees of freedom. The embedded region constraint option models a perfect bond between the concrete and reinforcement. This approach simulates the interaction by ensuring that translations and rotations are seamlessly transferred from the concrete to the reinforcement. It aligns the translational degrees of freedom at nodes on the embedded elements with those of the host elements, enabling unified behavior under applied loads.

The element types and reinforcement-concrete interaction are widely utilized in reinforced concrete modeling, as demonstrated by Dassault Systemes (2014) [22], and successfully applied by Madkour et al. (2022) [19], Nguyen & Livaoğlu (2020) [28] and Genikomsou & Polak (2015) [32].

The slabs were supported along all four edges, with the model replicating this condition by applying vertical restraints to simulate the actual support behavior. The load was introduced using a displacement-controlled protocol through a smooth step function, as shown in Figure 10, applied to a central node at the slab's midpoint. This node was coupled to the slab surface via a constraint that evenly distributed the displacement across the column surface, accurately mimicking the experimental load application using a hydraulic jack.



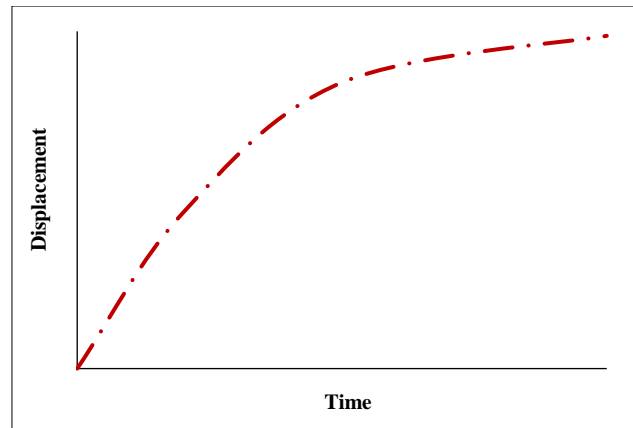


Figure 10. Smooth step loading function

### 4.3. Mesh Selection

Accurate simulation results depend on a refined mesh. While a fine mesh improves the precision of the localization band, it increases computational effort, requiring smaller increment sizes and potentially causing numerical convergence issues. Conversely, a coarse mesh reduces computational demand but may compromise result accuracy, as illustrated by Ren et al. (2014) [26].

A mesh convergence study is crucial to identify the optimal mesh size, involving a stepwise reduction in mesh size (increasing density) until further refinement produces negligible changes in the solution. Mesh sizes of 25 mm, 35 mm, and 45 mm were evaluated, as detailed in Table 3 and illustrated in Figure 11. The results indicate convergence in punching shear capacity across the mesh sizes, with 35 mm and 25 mm accurately capturing load capacity. This was further validated by comparing experimental and FEA load-deflection curves across the mesh sizes (Figure 11). Although 35 mm and 25 mm produced reliable results, the 25 mm mesh was selected for its higher precision with minimal additional computational demand.

Table 3. Mesh sensitivity analysis based on the punching shear capacity

Sample ID	Mesh size	$V_{FEA}$ (kN)	$V_{EXP.}$ (kN)	Difference %
G-30-1.8	25	126	124	1.8
	35	121		1.9
	45	114		7.6

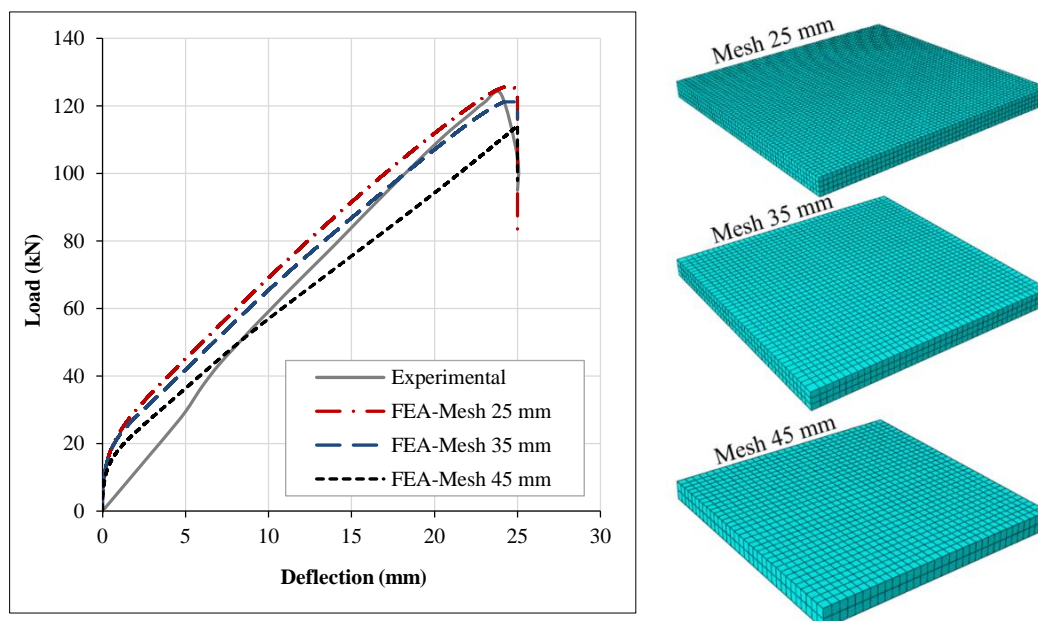


Figure 11. Load deflection curves for sample G-30-1.8 with different mesh sizes



The chosen mesh size of 25 mm aligns with those used in comparable simulations and sample sizes reported in the literature. Mesh sizes ranging from 20 to 50 mm were employed in studies by Madkour et al. (2022) [19], Genikomsou and Polak (2015) [32], and Demissie & Aure (2022) [34].

## 5. Experimental and FEA results

### 5.1. Failure Mode and Cracking Pattern

All tested slabs exhibited brittle punching shear failure, characterized by circumferential cracking and a sudden load drop. No flexural failure modes were observed, such as concrete crushing or GFRP bar rupture. Crack behavior was consistent across all specimens, with initial flexural cracks along the slab followed by radial cracks originating at the column face and propagating toward the slab edges and corners. As the load increased, additional radial cracks formed, and existing cracks widened until circumferential punching shear cracks developed, accompanied by a sudden load drop. Similar cracking patterns and failure mechanisms have been reported in previous studies by Al-Mamoori (2015) [35] and Benmokrane et al. (2006) [36]. Experimental and FEA cracking patterns, shown in Figure 12, demonstrate similar trends across all specimens. However, HSC specimens developed fewer, narrower cracks than NSC specimens, attributed to the higher modulus of elasticity in HSC, which delays crack initiation and limits flexural crack width.

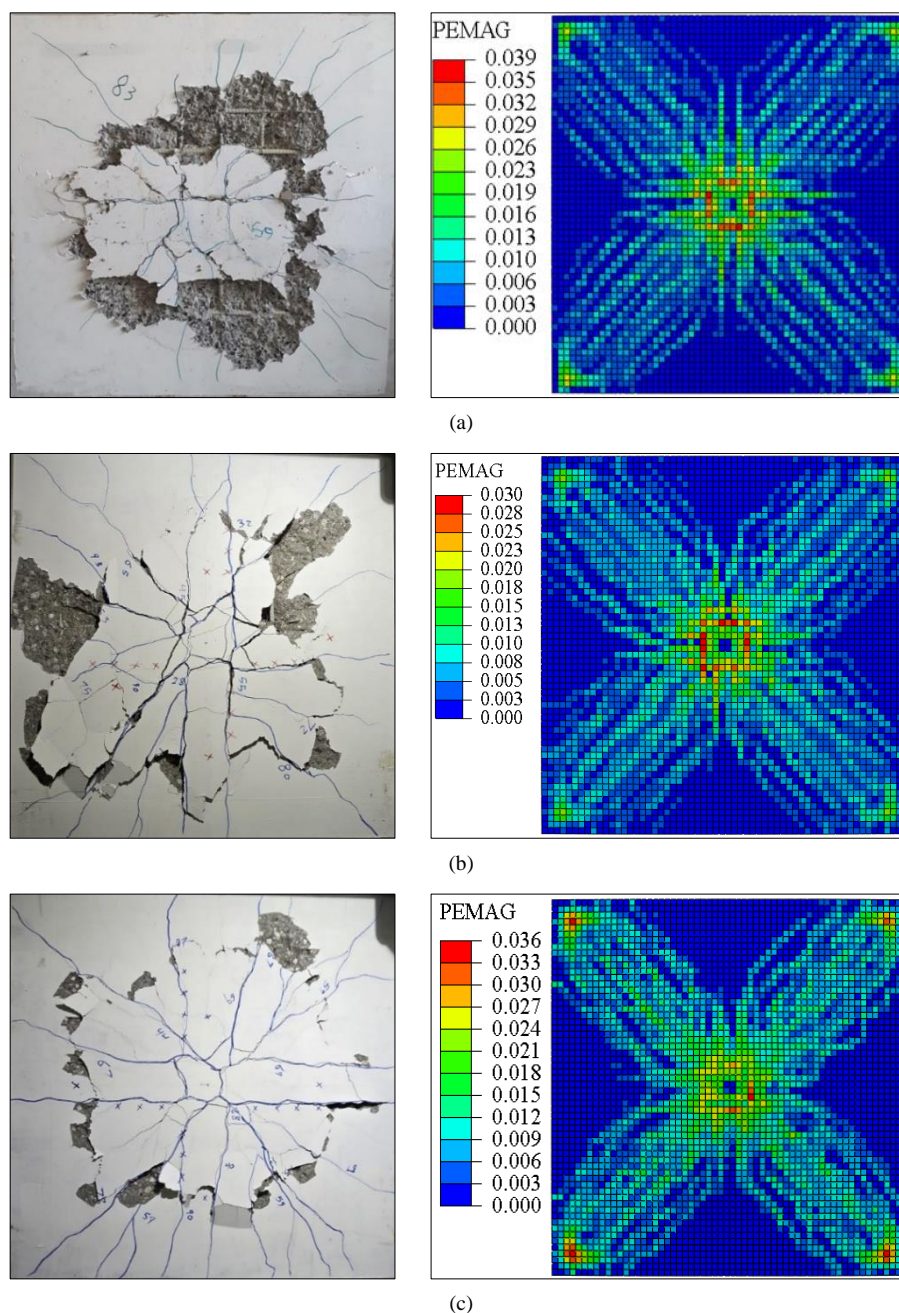
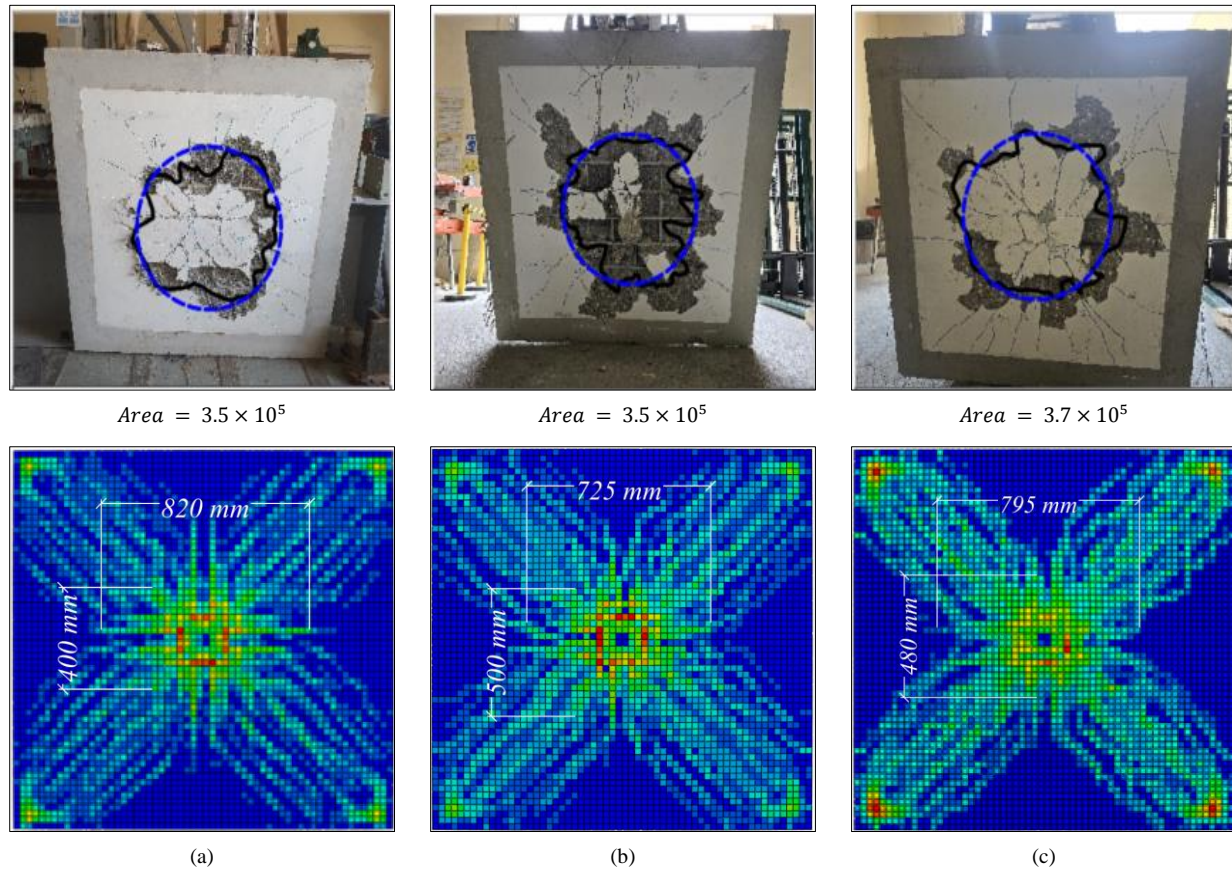


Figure 12. Experimental and FEA cracking pattern at failure for the tested specimens: (a) G-30-1.8, (b) G-60-1.8, and (c) G-90-1.8

The observed failure perimeter in the tested slabs was circular. To accurately identify the punching shear failure perimeter and angle, loose concrete fragments were removed post-testing, and the perimeter was determined from the termination points of diagonal cracks through the slab depth. Figure 13 compares the experimental and FEA failure perimeters.



**Figure 13. Punching shear failure area for the tested specimens: (a) C30-1.8, (b) C60-1.8, and (c) C90-1.8**

The experimental critical perimeter was calculated as the radius of an equivalent circle based on the observed failure area (blue circle). The FEA failure perimeter was determined by averaging the maximum and minimum crack extension distances, as shown in Figure 13. Results in Table 4 reveal strong agreement between experimental and FEA data, indicating that increased concrete strength slightly enlarges the failure perimeter radius. The failure angle remained consistent at approximately 16 degrees across all samples.

**Table 4. Punching shear failure location and angle for the tested specimens.**

Specimen ID	$L_f$	
	Experimental	FEA
G-30-1.8	3.4	3.5
G-60-1.8	3.5	3.5
G-90-1.8	3.6	3.7

## 5.2. Load-Deflection Curves and Capacity

The experimental and FEA load-deflection curves for the tested specimens are shown in Figure 14. All specimens exhibited a typical bilinear behavior, where the initial slope represents the initial stiffness, and the second slope indicates the post-cracking stiffness.

As shown in Figure 14, specimens with higher concrete strength demonstrated greater initial stiffness, attributable to their higher modulus of elasticity. For instance, C60 specimens, with a modulus of elasticity 1.9 times higher than C30 specimens, achieved a 38% increase in average initial stiffness (from 5.8 kN/mm for C30 to 8 kN/mm for C60). Similarly, the C90 specimen, with a modulus of elasticity 2.2 times that of C30, exhibited an initial stiffness of 8.9 kN/mm, a 53% increase compared to C30.

The load-deflection curves generated from the FEA align well with experimental results but exhibit a slightly stiffer response. This discrepancy is attributed to several factors, including microcracks in the experimental samples caused by drying, handling, and concrete shrinkage before testing, which reduce initial stiffness. Additionally, the FEA assumes a

perfect rigid bond between reinforcement and concrete, ignoring potential slippage that can reduce stiffness in experimental conditions. Similar observations and explanations have been reported by Madkour et al. (2022) [19], Nguyen and Livaoğlu (2020) [28], and Genikomsou and Polak (2015) [32].

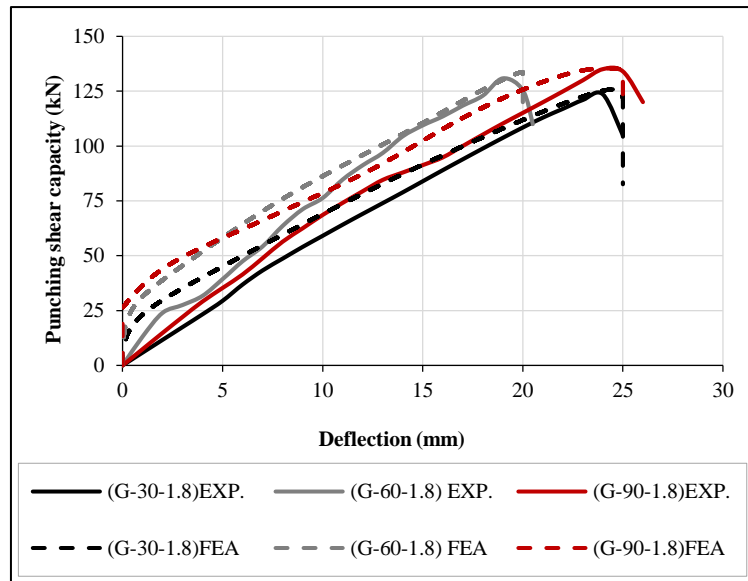


Figure 14. Experimental and FEA Load-deflection curves for NSC and HSC slabs

Using HSC improves punching shear capacity. Increasing concrete strength from C30 to C60 resulted in a 5.6% capacity enhancement; from C30 to C90, it achieved an 8.9% capacity increase. The FEA results closely match the experimental findings, with a maximum difference of only 2.9 % between the experimental and FEA, as shown in Table 5.

Table 5. Experimental and FEA punching shear capacity

Sample	$V_p$ (kN)		Difference %	$V_{EXP./FEA}$ -
	Exp.	FEA		
G-30-1.8	124	126	1.6	0.98
G-60-1.8	131	134	2.3	0.98
G-90-1.8	135	136	2.9	1.03

To evaluate the reinforcement contribution to punching shear resistance for NSC and HSC, the normalized punching shear capacity with respect to the concrete strength is plotted in Figure 15. The figure shows that reinforcement axial stiffness contribution to the punching shear resistance is more pronounced when NSC is used than HSC. This is due to the high elastic modulus of HSC, which approaches or exceeds that of the GFRP bars.

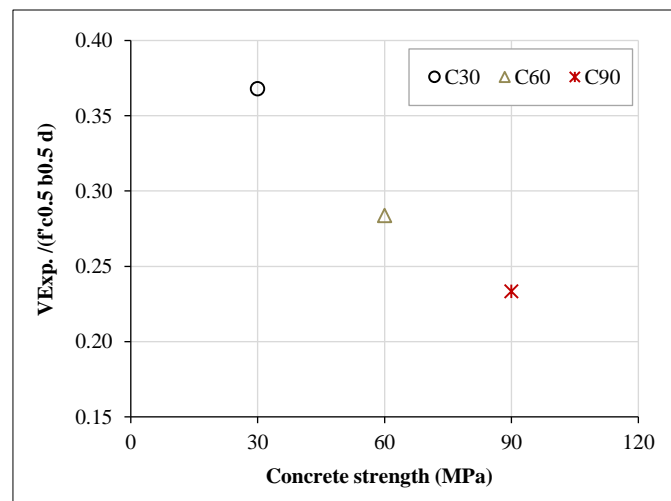


Figure 15. The normalized punching shear capacity for different concrete strengths

### 5.3. Strains Development

Figure 16 presents the reinforcement strain at a distance of 2d from the column face throughout the loading stages for the three tested specimens. The NSC specimen exhibited higher strain values than the HSC specimens, attributed to the higher stiffness of HSC, which transfers more forces to the concrete, reducing stress in the reinforcement. None of the reinforcement bars in the tested specimens ruptured, as confirmed by strain values below the ultimate tensile strain. Table 6 summarizes the experimental and FEA maximum strains at peak load and compares them to the ultimate tensile strain. The FEA strain results closely align with the experimental data, as shown in Figure 16 and Table 6, validating the accuracy of the developed FEA model in capturing the actual behavior.

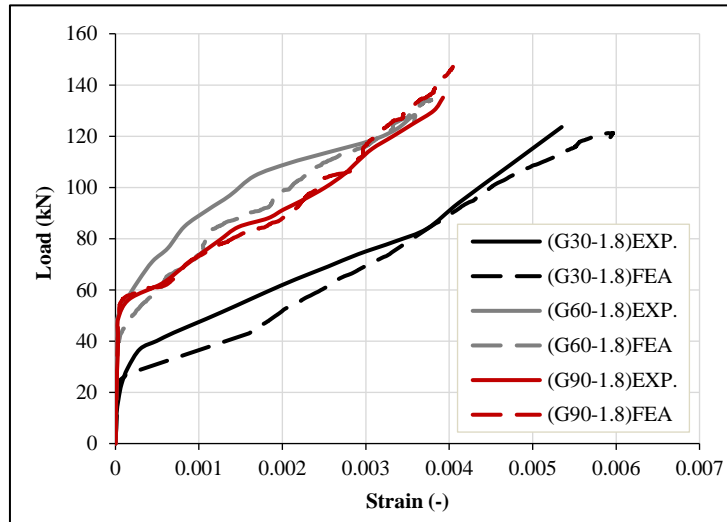


Figure 16. Experimental and FEA Load-strain curves for the tested samples

Table 6. Reinforcements strains at peak load at 2d from the face of the column

Sample	$\mu\epsilon_{peak}$		$(\epsilon_{peak}/\epsilon_u) \%$	
	Exp.	FEA	Exp.	FEA
G-30-1.8	5348	5961	32	36
G-60-1.8	3578	3785	21	23
G-90-1.8	3925	4045	24	24

### 6. Comparison with Code Predictions

Structural design codes and guidelines offer design expressions for estimating the punching shear resistance of GFRP-reinforced slabs such as those provided by ACI 440.11-22, JSCE-97, and CAN/CSA S806-12 [9-11] and summarized in Table 7. These equations are adaptations of those developed initially for traditional steel-reinforced slabs, modified to consider the unique physical and mechanical properties of FRP bars.

Table 7. Punching shear of FRP-reinforced slabs code prediction equations

Design Model	Punching Shear Equation ( $V_c$ )
ACI 440.11-22	$V_c = 0.83 \lambda_s k \sqrt{f'_c} b_{o,0.5d} d, \sqrt{f'_c} \leq 8.3 \text{ MPa}$
	$k = \sqrt{2\rho_f \frac{E_f}{E_c} + \left(\rho_f \frac{E_f}{E_c}\right)^2} - \rho_f \frac{E_f}{E_c}, \lambda_s = \sqrt{\frac{2}{1+0.004d}}$
	$v_c \text{ need not to be less than } 0.13\lambda_s \sqrt{f'_c}$
JSCE-97	$V_c = \beta_d \beta_p \beta_r f_{pcd} b_{o,0.5d} d$
	$\beta_d = \sqrt[4]{\frac{1}{d}} \leq 1.5, \beta_p = \sqrt[3]{100\rho_f \frac{E_f}{E_s}} \leq 1.5, \beta_r = 1 + \frac{1}{1+0.25\frac{b_{o,0.5d}}{d}}$
	$f_{pcd} = 0.2\sqrt{f'_{cd}} \leq 1.2$
CAN/CSA S806-12	$V_c = \min \left\{ \begin{array}{l} 0.028 \left(1 + \frac{2}{\beta_c}\right) (E_f \rho_f f'_c)^{\frac{1}{3}} b_{o,0.5d} d \\ 0.147 \left(0.19 + \frac{a_s d}{b_{o,0.5d}}\right) (E_f \rho_f f'_c)^{\frac{1}{3}} b_{o,0.5d} d \\ 0.056 (E_f \rho_f f'_c)^{\frac{1}{3}} b_{o,0.5d} d \end{array} \right\}$

$V_c$ : punching shear capacity (N),  $\rho_f$ : reinforcement ratio,  $E_f$ ,  $E_c$ ,  $E_s$ : FRP, concrete, and steel moduli of elasticity,  $f'_c$ : concrete strength (MPa),  $d$ : effective depth (mm),  $b_{o,0.5d}$  critical perimeters at 0.5d from the column face (mm),  $a_s$ : column location factor 2, 3, and 4 for corner, edge, and inner locations, and  $\beta_c$ : column aspect ratio.



To assess the accuracy of the design code equations, their predictions were compared with the experimentally and FEA-obtained punching shear capacities. Table 8 summarizes the ratios of experimental-to-predicted punching shear capacities ( $V_{Exp.}/V_{pred.}$ ) using the design formulations listed in Table 7 and the FEA results. For this comparison, resistance factors were omitted from all punching shear formulations.

**Table 8. Experimental-to-predicted ratios**

Specimen ID	$\rho_f$	$f'_c$	$E_f$	$E_c$	$d$	$b_{o,0.5d}$	$V_{Exp.}$	$V_{Exp.}/V_{pred.}$			
	-	MPa	GPa	GPa	mm	mm	kN	FEA	ACI 440.11-22		ACI 440.11-22
G-30-1.8	0.018	35	60	28	66	864	124	0.98	1.83	1.16	1.16
G-60-1.8	0.018	65	60	53	66	864	131	0.98	1.64	1.20	1.02
G-90-1.8	0.018	103	60	62	66	864	135	0.99	2.11	1.24	1.05
<b>Mean</b>								0.98	1.86	1.20	1.08
<b>COV %</b>								0.63	10.38	2.72	5.59

As shown in Table 8, the FEA and CAN/CSA S806-12 [11] code equations provided accurate predictions, with average experimental-to-predicted ratios of 0.98 and 1.08, respectively. The JSCE-97 [10] code predictions, while slightly more conservative, demonstrated greater consistency, yielding a coefficient of variation (COV) of 2.72%, compared to 5.59% for CAN/CSA S806-12 [11]. In contrast, the ACI 440.11-22 [9] code equation produced significantly more conservative predictions, with an average experimental-to-predicted ratio of 1.86 and a COV of 10.38%.

Although the FEA results provided the most accurate and least variable predictions, it is recommended that a resistance factor, similar to those applied in design codes, be incorporated into FEA-based predictions to ensure safe and reliable designs.

## 7. Conclusions

This study used experimental and numerical approaches to examine the punching shear behavior of Glass Fiber-Reinforced Polymer (GFRP)-reinforced concrete slabs. Three full-scale slab specimens with varying concrete strengths (30, 60, and 90 MPa) were tested under concentric loading to investigate the influence of concrete strength on punching shear capacity. Finite Element Analysis (FEA) using the Concrete Damage Plasticity (CDP) model in ABAQUS was employed to simulate the experimental tests and provide deeper insights into crack development, failure modes, and load-deflection behavior. The key findings are summarized as follows:

- Increasing the concrete strength from 30 MPa to 60 MPa and 90 MPa enhanced the punching shear capacity by 5.6% and 8.9%, respectively.
- High-strength concrete (HSC) demonstrated superior stiffness, reducing reinforcement strain and delaying crack propagation compared to normal-strength concrete (NSC).
- The developed FEA model accurately captured experimental results, including load-deflection behavior, crack patterns, and failure mechanisms. The maximum deviation between experimental and numerical results was less than 3%, confirming the model's reliability for analyzing GFRP-reinforced slabs.
- All slabs exhibited brittle punching shear failure characterized by circumferential cracking around the column face. The experimental and FEA results indicated that the critical failure perimeter was approximately 3.5 times the slab depth from the column face.
- The contribution of reinforcement stiffness to punching shear resistance was more pronounced in NSC slabs due to the relatively lower modulus of elasticity of NSC compared to HSC.

## 8. Declarations

### 8.1. Author Contributions

Conceptualization, S.B.; methodology, A.A. and R.A.; software, A.A.; writing—original draft preparation, A.A.; writing—review and editing, R.A.; supervision, S.A., M.T.J., and M.M. All authors have read and agreed to the published version of the manuscript.

### 8.2. Data Availability Statement

The data presented in this study are available on request from the corresponding author.

### 8.3. Funding

This research was supported by The College of Graduate Studies and Research and The Sustainable Construction Materials and Structural Systems (SCMASS) research group at the University of Sharjah, United Arab Emirates. This support is highly appreciated.

#### 8.4. Acknowledgements

Gratitude is extended to Emirates Stone and CONMIX for their supply of materials, technical assistance, and collaborative efforts during the casting process and to Mateenbar for providing the GFRP reinforcement bars.

#### 8.5. Conflicts of Interest

The authors declare no conflict of interest.

### 9. References

- [1] ACI-440.1R-15. (2015). Guide for the Design and Construction of Structural Concrete Reinforced with Fiber-Reinforced Polymer (FRP) Bars. American Concrete Institute (ACI), Michigan, United States.
- [2] Benmokrane, B., Ahmed, E., Dulude, C., & Boucher, E. (2012). Design, construction, and monitoring of the first worldwide two-way flat slab parking garage reinforced with GFRP bars. *Proceedings of the International conference on Composites in Civil Engineering CICE*, 13-15 June, Rome, Italy.
- [3] Salama, A. E., Hassan, M., Benmokrane, B., & Ferrier, E. (2020). Modified strip model for punching-shear strength of FRP-reinforced concrete edge-column slab connections. *Engineering Structures*, 216, 110769. doi:10.1016/j.engstruct.2020.110769.
- [4] Nguyen-Minh, L., & Rovňák, M. (2013). Punching Shear Resistance of Interior GFRP Reinforced Slab-Column Connections. *Journal of Composites for Construction*, 17(1), 2–13. doi:10.1061/(asce)cc.1943-5614.0000324.
- [5] Ju, M., Park, K., & Park, C. (2018). Punching shear behavior of two-way concrete slabs reinforced with glass-fiber-reinforced polymer (GFRP) bars. *Polymers*, 10(8), 893. doi:10.3390/polym10080893.
- [6] Duan, N., & Zhang, J. (2024). The Impact of Reinforcement Ratio on the Punching Shear of CFRP Grid-Reinforced Concrete Two-Way Slabs. *Materials*, 17(22), 5576. doi:10.3390/ma17225576.
- [7] Talha Junaid, M., Awad, R., Barakat, S., & Metawa, A. (2024). Effect of column dimension on the punching shear capacity of concrete slabs reinforced with GFRP bars. *E3S Web of Conferences*, 586, 4003. doi:10.1051/e3sconf/202458604003.
- [8] Alkhatabi, L., Ayash, N. M., Hassan, M., & Gouda, A. (2024). Investigation of Key Parameters Influencing Shear Behavior in Glass-Fiber-Reinforced Polymer (GFRP)-Reinforced Concrete (RC) Interior Slab-Column Connections. *Buildings*, 14(5), 1251. doi:10.3390/buildings14051251.
- [9] ACI Code-440.11-22. (2022). Building Code Requirements for Structural Concrete and Commentary. American Concrete Institute (ACI), Michigan, United States.
- [10] CSA S806-12. (2012). Design and Construction of Building Structures with Fiber Reinforced Polymers. Canadian Standards Association (CSA), Toronto, Canada.
- [11] JSCE. (19997). Recommendation for design and construction of concrete structures using continuous fiber reinforcing materials. Japan Society of Civil Engineers (JSCE), Tokyo, Japan.
- [12] Lee, J. H., Yang, J. M., & Yoon, Y. S. (2010). Rational prediction of punching shear strength of slabs reinforced with steel or FRP bars. *Magazine of Concrete Research*, 62(11), 821–830. doi:10.1680/mac.2010.62.11.821.
- [13] Hassan, M., Ahmed, E. A., & Benmokrane, B. (2015). Punching Shear Behavior of Two-Way Slabs Reinforced with FRP Shear Reinforcement. *Journal of Composites for Construction*, 19(1). doi:10.1061/(asce)cc.1943-5614.0000493.
- [14] Hassan, M., Ahmed, E., & Benmokrane, B. (2013). Punching-Shear Strength of Normal and High-Strength Two-Way Concrete Slabs Reinforced with GFRP Bars. *Journal of Composites for Construction*, 17(6), 4013003. doi:10.1061/(asce)cc.1943-5614.0000424.
- [15] Zhang, Q., Marzouk, H., & Hussein, A. (2005). A preliminary study of high-strength concrete two-way slabs reinforced with GFRP bars. *Proceedings of the 33<sup>rd</sup> CSCE annual conference: general conference and international history symposium*, 2-4 June, 2005, Toronto, Canada.
- [16] Hussein, A. H., & El-Salakawy, E. F. (2018). Punching shear behavior of glass fiber-reinforced polymer-reinforced concrete slab-column interior connections. *ACI Structural Journal*, 115(4), 1075–1088. doi:10.14359/51702134.
- [17] Xu, W., & Shi, X. (2024). Machine-Learning-Based Predictive Models for Punching Shear Strength of FRP-Reinforced Concrete Slabs: A Comparative Study. *Buildings*, 14(8), 2492. doi:10.3390/buildings14082492.
- [18] Alateyat, A., Awad, R., Ibrahim, B., Junaid, M. T., Altoubat, S., Maalej, M., & Barakat, S. (2024). Punching shear strength of fiber-reinforced polymer concrete slabs: Database-driven assessment of parameters and prediction models. *Engineering Structures*, 315, 118511. doi:10.1016/j.engstruct.2024.118511.
- [19] Madkour, H., Maher, M., & Ali, O. (2022). Finite element analysis for interior slab-column connections reinforced with GFRP bars using damage plasticity model. *Journal of Building Engineering*, 48, 104013. doi:10.1016/j.job.2022.104013.

- [20] Al-Rousan, R. Z., Alhassan, M., & Al-wadi, R. (2020). Nonlinear finite element analysis of full-scale concrete bridge deck slabs reinforced with FRP bars. *Structures*, 27, 1820–1831. doi:10.1016/j.istruc.2020.08.024.
- [21] ASTM D8505/D8505M-23. (2023). Standard Specification for Basalt and Glass Fiber Reinforced Polymer (FRP) Bars for Concrete Reinforcement. ASTM International, Pennsylvania, United States. doi:10.1520/D8505\_D8505M-23.
- [22] ABAQUS. (2014). Abaqus analysis user's guide. Dassault Systèmes, Vélizy-Villacoublay, France.
- [23] Voyiadjis, G. Z., & Taqieddin, Z. N. (2009). Elastic plastic and damage model for concrete materials: Part I-theoretical formulation. *The International Journal of Structural Changes in Solids*, 1(1), 31-59.
- [24] Jankowiak, T., & Lodygowski, T. (2005). Identification of parameters of concrete damage plasticity constitutive model. *Foundations of civil and environmental engineering*, 6(1), 53-69.
- [25] Vojdan, B. M., & Aghayari, R. (2017). Investigating the seismic behavior of RC shear walls with openings strengthened with FRP sheets using different schemes. *Scientia Iranica*, 24(4), 1855–1865. doi:10.24200/sci.2017.4276.
- [26] Ren, W., Sneed, L. H., Yang, Y., & He, R. (2015). Numerical Simulation of Prestressed Precast Concrete Bridge Deck Panels Using Damage Plasticity Model. *International Journal of Concrete Structures and Materials*, 9(1), 45–54. doi:10.1007/s40069-014-0091-2.
- [27] Surumi, R. S., Jaya, K. P., & Greeshma, S. (2015). Modelling and Assessment of Shear Wall–Flat Slab Joint Region in Tall Structures. *Arabian Journal for Science and Engineering*, 40(8), 2201–2217. doi:10.1007/s13369-015-1720-z.
- [28] Nguyen, Q. T., & Livaoğlu, R. (2020). The effect of the ratio of  $\Lambda$ -shaped shear connectors on the flexural behavior of a reinforced concrete frame. *Advances in Structural Engineering*, 23(12), 2724–2740. doi:10.1177/1369433220920442.
- [29] Popovics, S. (1973). A numerical approach to the complete stress-strain curve of concrete. *Cement and Concrete Research*, 3(5), 583–599. doi:10.1016/0008-8846(73)90096-3.
- [30] Hsu, L. S., & Hsu, C. T. T. (1994). Complete stress – strain behaviour of high-strength concrete under compression. *Magazine of Concrete Research*, 46(169), 301–312. doi:10.1680/mac.1994.46.169.301.
- [31] Cornelissen, H. A. W., Hordijk, D. A., & Reinhardt, H. W. (1986). Post-Peak Tensile Behaviour of Lightweight versus Normal-Weight Concrete. *Brittle Matrix Composites 1*, 1, 509–525. doi:10.1007/978-94-009-4319-3\_34.
- [32] Genikomsou, A. S., & Polak, M. A. (2015). Finite element analysis of punching shear of concrete slabs using damaged plasticity model in ABAQUS. *Engineering Structures*, 98, 38–48. doi:10.1016/j.engstruct.2015.04.016.
- [33] Carreira, D. J., & Chu, K. H. (1986). Stress-Strain Relationship for Reinforced Concrete in Tension. *Journal of the American Concrete Institute*, 83(1), 21–28. doi:10.14359/1756.
- [34] Demissie, G. A., & Aure, T. W. (2022). Numerical analysis of GFRP-reinforced flat slab–column edge connection subjected to gravity and lateral loads. *Asian Journal of Civil Engineering*, 23(5), 765–783. doi:10.1007/s42107-022-00456-6.
- [35] Al-Mamoori, A. H. N. (2015). Investigation the punching shear behavior of reinforced concrete slab-column connection using carbon fiber reinforced polymers. *Al-Qadisiya Journal for Engineering Science*, 8(1), 38-58.
- [36] Benmokrane, B., Masmoudi, R., & El-Salakawy, E. (2004). Designing and testing of a concrete bridge deck reinforced with glass FRP bars. *International SAMPE Technical Conference*, 11(2), 2815–2828. doi:10.1061/(asce)1084-0702(2006)11:2(217).